Inorganic Chemistry

Article

pubs.acs.org/IC

Influence of Sequential Thiolate Oxidation on a Nitrile Hydratase Mimic Probed by Multiedge X-ray Absorption Spectroscopy

Jason Shearer,*[,†] Paige E. Callan,[†] César A. Masitas,[‡] and Craig A. Grapperhaus*[,‡]

[†]Department of Chemistry, University of Nevada, Reno, Nevada 89557, United States

[‡]Department of Chemistry, University of Louisville, Louisville, Kentucky 40292, United States

Supporting Information

ABSTRACT: Nitrile hydratases (NHases) are Fe(III)- and Co(III)-containing hydrolytic enzymes that convert nitriles into amides. The metal-center is contained within an N_2S_3 coordination motif with two post-translationally modified cysteinates contained in a *cis* arrangement, which have been converted into a sulfinate ($R\text{-}SO_2^-$) and a sulfenate ($R\text{-}SO^-$) group. Herein, we utilize Ru L-edge and ligand (N-, S-, and P-) K-edge X-ray absorption spectroscopies to probe the influence that these modifications have on the electronic structure of a series of sequentially oxidized thiolate-coordinated Ru(II) complexes ((bmmp-TASN)$RuPPh_3$, (bmmp-O_2-TASN)$RuPPh_3$, and (bmmp-O_3-TASN)$RuPPh_3$). Included is the use of N K-edge spectroscopy, which was used for the first time to extract N-metal covalency parameters. We find that upon oxygenation of the bis-thiolate compound (bmmp-TASN)$RuPPh_3$ to the sulfenato species (bmmp-O_2-TASN)$RuPPh_3$ and then to the mixed sulfenato/sulfinato speices (bmmp-O_3-TASN)$RuPPh_3$ the complexes become progressively more ionic, and hence the Ru^{II} center becomes a harder Lewis acid. These findings are reinforced by hybrid DFT calculations (B(38HF)P86) using a large quadruple-ζ basis set. The biological implications of these findings in relation to the NHase catalytic cycle are discussed in terms of the creation of a harder Lewis acid, which aids in nitrile hydrolysis.

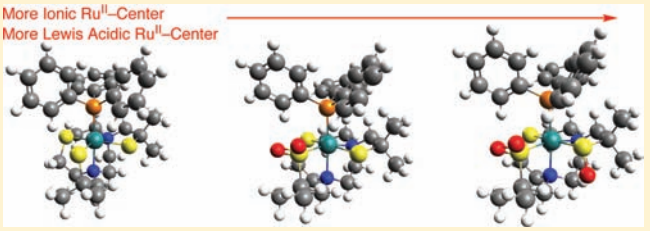

INTRODUCTION

Nitrile hydratases (NHases) are mononuclear nonheme Fe(III) or noncorrinoid Co(III)-containing metalloenzymes that convert nitriles into amides (Figure 1a).[1−5] A closely related

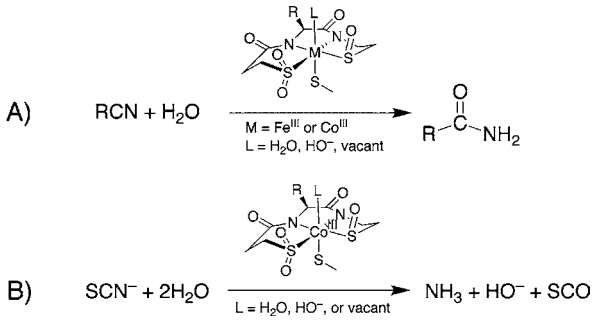

Figure 1. (A) Reaction catalyzed by nitrile hydratases and (B) reaction catalyzed by thiocyanate hydrolase. Note the similarity in active-site structures.

class of metalloenzymes are the thiocyanate hydrolayses (SNCase), which hydrolyze the thiocyanate anion into SCO and NH_3 (Figure 1b).[6−8] The metal ions found at the NHase and SCNase active sites are redox inactive and are thought to behave as Lewis acids in the catalytic cycle. Both classes of metalloenzymes contain the metal ion within an N_2S_3 coordination motif with the nitrogen ligands derived from deprotonated amide nitrogens from the peptide backbone and the sulfur-based ligands derived from cysteinate residues.[7−14] The two *cis*-cysteinates that are *trans* to the amidate nitrogens have been post-translationally modified to a sulfinate ($R\text{-}SO_2^-$) and a sulfenate ($R\text{-}SO^-$) ligand. The role that the oxygenated cysteinates[15] play in controlling the electronic properties of the metal ions in these metalloenzymes has been the subject of a number of studies.[9,14,16−24]

A number of enzymatic, spectroscopic, and modeling studies have demonstrated that these modified cysteinates are required for enzymatic activity in both NHase and SCNase.[1,9,14,16−24] Solomon and co-workers have suggested that thiolate oxygenation in Fe-containing NHase will increase the Lewis-acidity of the metal center compared with the analogous active-site containing unmodified thiolates.[16] This occurs *via* a reduction in the covalency of the $M\text{−}SO_2$ bond, which is mostly but not entirely compensated for by a subsequent increase in the covalency of the unmodified M−S bond.[16,17] Similar findings have been reached by Shearer and co-workers on Co-containing NHase peptide-based models.[24]

Prior to the discovery that NHase contained oxygenated thiolates, it was assumed that oxygen exposure to Fe(III) thiolates largely results in thiolate oxidation, proceeded by disulfide bond formation and the subsequent decomposition of the transition-metal complex. Thus, preparation of discrete model compounds for NHase-containing metal centers

Received: November 14, 2011
Published: May 16, 2012

   dx.doi.org/10.1021/ic202453c | *Inorg. Chem.* 2012, 51, 6032−6045

Chart 1

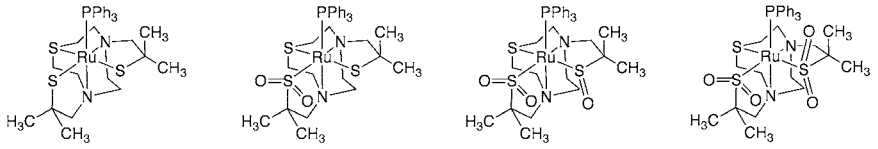

coordinated by oxygenated ligands became a subject of intense investigation.[1,25−36] These studies have shown that sulfur−oxygenation of iron−thiolates by dioxygen can be readily accomplished by use of an iron−thiolate precursor in a low-spin configuration. The low-spin configuration results in high M−S covalency, which in turn favors S-oxygenation over thiolate one-electron oxidation.[36] These results led one of us to investigate the oxygen sensitivity of a low-spin Ru(II) derivative of the NHase model complex (bmmp-TASN)FeCl (Chart 1).[37−39] Oxygenation of (bmmp-TASN)$RuPPh_3$ (RuS) under limiting O_2 conditions can be readily effected and *controlled* yielding a unique "family" of complexes that differ only in the degree of S-oxygenation. By controlling the oxygenation conditions, the monosulfinato (bmmp-O_2-TASN)$RuPPh_3$ ($RuSO_2$), the mixed sulfenato/sulfinato complex (bmmp-O_3-TASN)$RuPPh_3$ ($RuSO_2$/SO), and the bissulfinato (bmmp-O_4-TASN)$RuPPh_3$ ($RuSO_2/SO_2$) are all accessible.[39] The physical properties of these compounds display systematic differences as the S-based ligands become successively oxygenated, including an increase in the Ru−P bond length. This result seemed counterintuitive as one may suspect that a reduction in the covalency of the Ru−SO_2 and Ru−SO bonds would presumably be compensated for by an increase in the covalency of the Ru−P bond.

Although a number of metal S-oxygenates have been reported, families of complexes containing three or more oxygenated derivatives are rare. Thus far, only the (bmmp-TASN)$RuPPh_3$ family contains variable ligand sites within a complex that retains the same geometry throughout the series.[31] These compounds provide us with a unique opportunity to probe the electronic structure of successively oxygenated NHase model compounds to better understand the influence of thiolate oxygenation on thiolate-rich low-spin transition metal compounds. In this study, we utilize multiple edge X-ray absorption spectroscopy (XAS), in which each ligating atom type and the Ru center are probed. Thus, we can investigate in detail the changes in the electronic structure of the metal complexes upon thiolate oxygenation in the complexes RuS, $RuSO_2$, and $RuSO_2$/SO. Included is the use of N K-edge spectroscopy, which as far as we can tell, has not been utilized to extract covalency parameters in transition metal complexes prior to this study. We will demonstrate that the sequential oxygenation of the thiolates results in a dramatic reduction of the covalency of these complexes and results in a harder Ru center. The consequences of these changes on NHase catalysis will be discussed in terms of the creation of a better Lewis acid at the active site, which in turn enhances catalytic activity.

EXPERIMENTAL SECTION

Model Complex Synthesis. The complexes (bmmp-TASN)-$RuPPh_3$, (bmmp-O_2-TASN)$RuPPh_3$, and (bmmp-O_3-TASN)$RuPPh_3$ were prepared according to previously published methods.[38,39] All samples were purified by crystallization, and bulk purity was assessed by squarewave voltammetry. Manipulations were subsequently performed using inert-atmosphere techniques.

X-Ray Absorption Spectroscopy: Sample Preparation and Data Collection. Under an atmosphere of dinitrogen in a glovebox, the transition metal complexes were finely ground. The resulting powders were then spread onto Kapton tape, forming thin layers. These films were then placed in lucite sample holders with polyethylene windows (3 μm thickness) that had been adhered to the sample holders with an epoxy resin. Data were collected at room temperature in a continuously purged He chamber on beamline X19a at the National Synchrotron Light Source (Brookhaven National Laboratories, Upton, New York) in an apparatus that has been previously described.[40] All S and P data were collected from 100 eV below the edge to 200 eV above the edge to ensure a good baseline fit. In the pre-edge region (100−30 eV below the edge), data were collected in 5 eV steps. In the edge region (30 eV below the edge to 5 eV above the edge), data were collected in 0.1 eV steps. In the near edge region (5−100 eV above the edge), data were collected in 1 eV steps, and in the far edge region (100−200 eV above the edge), data were collected in 2 eV steps. All Ru L-edge data were collected in 5 eV steps from 2635 to 2830 eV, 0.1 eV steps from 2830 to 2870 eV, 0.5 eV steps from 2870 to 2950 eV, 0.1 eV steps from 2950 to 3000, and 2 eV steps from 3000 to 3200 eV. S, P, and Ru spectra were calibrated to the peak maxima of the first pre-edge feature of $Na_2SO_4 \cdot 5H_2O$ (E = 2472.0 eV),[41] PPh_3O (E = 2147.5 eV),[42] and $Ru(bipy)_3Cl_2$ (L_3-edge maxima; E = 2840.5 eV),[43] respectively. All spectra represent the averaged sum of five scans.

All N K-edge data were obtained on beamline U4b at the National Synchrotron Light Source (Brookhaven National Laboratories, Upton, New York) using the previously described experimental setup.[45] Under an atmosphere of dinitrogen in an inert atmosphere glovebox, the metal complexes were finely ground and applied to double-sided carbon tape (SPI Supplies). These were then adhered to a sample paddle and lowered into the UHV chamber. All data were obtained in total electron yield mode at ambient temperature under a vacuum of less than 5×10^{-8} mbar. Data were collected in 2 eV steps prior to the edge region (350−390 eV), 0.1 eV steps in the edge region (390−410 eV), 0.5 eV steps in the near-edge region (410−420 eV), and 2 eV steps beyond the edge (420−450 eV). Charging effects for these compounds were not observed. All spectra represent the averaged sum of 10 scans. Data were calibrated to the first peak maximum of protoporphyrin-IX (399.0 eV).[44]

K-Edge X-Ray Absorption Data Workup and Analysis. After inspecting each scan, the data were averaged, and a basline was applied to each spectrum by fitting the pre-edge region to a polynomial function, which was subtracted from the spectrum. The region above the edge was then fit to a two knot cubic spline and the data normalized to the edge height. Depending on the number of oxidized sulfurs, up to three edge jumps were incorporated into the S K-edge data analysis. The nitrogen and phosphorus K-edge data required one edge jump. Pre-edge and edge transitions were modeled as pseudo-Voigt line shapes (1:1 Gaussian/Lorentzian line shapes). Extraction of individual transitions from the edge spectra used a procedure similar to that outlined and implemented by Kennepohl in his *Blueprint XAS* program.[46,47] A set of initial conditions were selected that included edge jump(s)/position(s)/height(s), the number of peaks along with peak-width-at-half-height to be included in the fit, and the energies of these peaks. The software then varies these initial conditions using a

dx.doi.org/10.1021/ic202453c | *Inorg. Chem.* 2012, 51, 6032−6045

Monte Carlo algorithm. Refinement of the data was achieved along with a simultaneous fitting of the baseline to ensure the baseline fit was not biasing the resulting fits to the transitions. In all, each model was arrived at by considering an array of 100 different initial condition parameters. Final models to the XAS data from these 100 different fits were arrived at by scoring the experimental vs simulated data using a simple χ^2 statistical analysis.[86] Because of the multiple peaks in the S K-edge spectra of the three complexes, this procedure was repeated 75 times (for a total of 7500 individual fits) to ensure the fidelity of the fits reported. As the differences in the values obtained for the final fits varied by less than 2% from one fit to another, the 75 individual "best fits" were averaged and used as the final reported model. A similar approach was used for the N and P K-edge data where only 25 repetitions of this procedure were required. All S pre-edge intensities were converted into %S(3p) character using Ni(DACO) as a standard (37.7(2)% S(3p) character per 100(1)% peak area (% eV relative to the edge)).[40,48] All N pre-edge peak intensities were converted into % N(2p) character using (bmmp-dmed)Ni as a standard (15.0(2)% N(2p) per 100(1)% peak area (% eV relative to the edge; see Figure S-1 and discussion of N K-edge spectra)). All %np ligand covalencies are reported per ligating atom type.

Ru L-Edge Data X-Ray Absorption Data Workup and Analysis. The L-edge spectra were individually inspected, summed, and averaged and the baseline (a polynomial function applied before the L_3 edge) subtracted from the spectrum. Two edge jumps and a two-knot cubic spline in the post L_2 edge region were subtracted from the spectra as well. The edge-jumps took on the form

$$I_n = H_n\left[\frac{1}{2} + \frac{1}{\pi}\arctan\left(\frac{E - P_n}{\Gamma/2}\right)\right] \quad (1)$$

where n = 2 or 3 (signifying the Ru L_2 or L_3 edge), H_n is the height of the edge jump, P_n is the inflection point position of the edge jump, and Γ is the width of the edge jump. Peak maxima were selected as the inflection points.

All spectra were simulated using de Groot's CTM4XAS package (Utrecht University, Utrecht, The Netherlands).[49] In the simulations of the Ru L-edge spectra, the atomic spectra are first calculated with an 80% reduction in the relevant Slater−Condon integrals to (partially) account for covalency. The atomic Hamiltonian is further extended using a crystal-field model using nominal C_4 symmetry resulting in energies for $10D_q$, D_s, and D_t.[73] Additional charge-transfer effects were included using a valence bond configuration interaction model[74] where the ground state is comprised of a linear combination of the Ru($4d^6$) configuration and the Ru($4d^7$)$\underline{L}$ charge transfer state (where $\underline{L}$ represents a ligand-based hole). The wave functions for these two states (Ψ_{GS} for the ground state wave function and Ψ_{CT} for the ligand to metal charge transfer (LMCT) state wave function) and the Hamiltonian (H) are described by

$$\Psi_{GS} = \alpha_o|4d^6\rangle + \beta_o|4d^7\underline{L}\rangle \quad (2)$$

$$\Psi_{CT} = \beta_o|4d^6\rangle - \alpha_o|4d^7\underline{L}\rangle \quad (3)$$

$$H = \begin{vmatrix} 0 & T \\ T & \Delta \end{vmatrix} \quad (4)$$

where Δ is the energy that separates the ground state and LMCT state configurations, ($\alpha_o^2 + \beta_o^2 = 1$) and T is a transfer integral that reflects the overlap between Ru and ligand-based orbitals.[75−77] As these complexes are represented as being C_4 symmetric, there are four transfer integrals (T_{B_1}, T_{A_1}, T_E, and T_{B_2}) representing the differential overlap between the four sets of Ru 4d orbitals and ligand-based orbitals.[78] The excited states can be described in an analogous manner by

$$\Psi_{ES1} = \alpha|\underline{2p}4d^7\rangle + \beta|\underline{2p}4d^8\underline{L}\rangle \quad (5)$$

$$\Psi_{ES2} = \beta|\underline{2p}4d^7\rangle - \alpha|\underline{2p}4d^8\underline{L}\rangle \quad (6)$$

$$H = \begin{vmatrix} 0 & T_f \\ T_f & \Delta_f \end{vmatrix} \quad (7)$$

The excited state transfer integral, T_f, is set equal to the ground state transfer integral in these simulations. Δ_f, the energy difference between Ψ_{ES1} and Ψ_{ES2}, is described by

$$\Delta_f = \Delta + Q - U \quad (8)$$

where Q and U are integrals representing 2p/4d and 4d/4d Coulombic interactions. The simulated spectra are convolutions of 85% Gaussian (for instrumental line broadening effects) and 15% Lorentzian (for lifetime line broadening effects) line shape with line widths of 1.15 eV applied to each transition. The above parameters are systematically varied until a best fit to the data is achieved using a χ^2 scoring scheme.

Electronic Structure Calculations. All electronic structure calculations were performed using Neese's electronic structure package ORCA v. 2.8 (Universität Bonn; Bonn, Germany).[50] In all cases, the complete structures of (bmmp-TASN)$RuPPh_3$, (bmmp-O_2-TASN)-$RuPPh_3$, and (bmmp-O_3-TASN)$RuPPh_3$ were utilized. All ground-state density functional theory (DFT) calculations employed either Ahlrichs' TZVPP or def2-QZVPP basis set on all atoms,[51−54] a fine integration grid (ORCA Grid4), and tight SCF covergence criteria (ORCA VeryTightSCF convergence criteria). Initial geometry optimizations (GOs) were performed using Adamo and Barone's modification to the exchange and correlation functional of Perdew and co-workers and the TZVPP basis set.[55,56] Final GOs were performed using the spectroscopically adjusted hybrid density functional suggested by Szilagyi and co-workers (B(38HF)P86) and the TZVPP basis set.[57] Structures were considered converged if the energy change was less than 5×10^{-6} E_h, the gradient norm and maximum gradient elements were smaller than 1×10^{-4} E_h $Bohr^{-1}$ and 3×10^{-4} E_h $Bohr^{-1}$, the RMS displacement of all atoms was smaller than 2×10^{-3} Bohr, and the maximum displacement of any atom was smaller than 4×10^{-3} Bohr. Final single point calculations utilized the B(38HF)P86 hybrid functional and the def2-QZVPP basis set. Atomic orbital contributions to the resulting molecular orbitals were determined from a Löwden population analysis.[97] Isosurface plots were prepared using the computer program Molekel.[58] A natural bonding orbital analysis was performed using NBO v. 5.0[59] on the final B(38HF)P86/def2-QZVPP calculated electronic structures.

N and P ligand K-edge X-ray absorption pre-edge features were calculated using a time dependent density functional theory (TD-DFT) methodolgy and the def2-TZVP(-f) basis set.[60,61] All calculations employed the B3LYP hybrid functional,[62−65] the RIJCOSX approximation,[66−68] a fine integration grid, and tight SCF convergence criteria (ORCA Grid4; ORCA VeryTightSCF convergence criteria), with relativistic effects included using the scalar relativistic zeroth-order regular approximation (ZORA).[69,70] Use of ZORA had a minimal influence on the resulting energies. The first 30 lowest energy spin allowed transitions were calculated. For the N K-edge spectra, a 20.5 eV red shift was applied to all transition energies, while a 26.3 eV red shift was applied to all calculated P K-edge transitions. Transition intensities were scaled to best approximate the pre-edge, and the edges were approximated as sums of pseudo-Voigt peaks (1:1 Gaussian/Lorentzian line shapes) with a consistent peak width at half height of 0.75 eV for the N K-edge spectra and a 1.0 eV peak width for P K-edge spectra.

RESULTS AND DISCUSSION

In this study, the three ruthenium complexes (bmmp-TASN)$RuPPh_3$ (RuS), (bmmp-O_2-TASN)Ru-PPh_3 ($RuSO_2$), and (bmmp-O_3-TASN)$RuPPh_3$ ($RuSO_2$/SO) were investigated. The bis-sulfinate compound (bmmp-O_4-TASN)$RuPPh_3$ degrades slightly following isolation and was therefore not subjected to investigation in this study. Much of the interpretation of the ligand K-edge X-ray absorption spectro-

dx.doi.org/10.1021/ic202453c | Inorg. Chem. 2012, 51, 6032−6045

scopic data involves the use of spectra simulated using time-dependent density functional theory (TD-DFT). Thus, we begin by explaining how the DFT generated structures of RuS, $RuSO_2$, and $RuSO_2$/SO used throughout this study were produced and how they compare with the experimental structures.

Geometry Optimizations. To evaluate the X-ray absorption data presented below, a series of hybrid density functional calculations were performed on the three Ru complexes investigated. Final geometry optimizations were performed using the B(38HF)P86 hybrid density functional suggested by Solomon and co-workers.[57] This functional was originally developed to best match observable spectroscopic properties of the anion $(CuCl_4)^{2-}$ with its resulting computational parameters. It has been shown that this functional is capable of accurately determining the geometries, potential energy surfaces, and orbital contribution to the subsequent MOs for copper-containing transition metal complexes. Herein, we find that it is also capable of accurately describing the geometry and electronic structure of these Ru(II)-containing complexes as well.

Table 1 gives selected metric parameters comparing the calculated structures (B(38HF)P86/TZVPP) vs experimentally

Table 1. Comparison of Selected Experimental (X-Ray Crystallography) vs Calculated (B(HF38)P86/TZVPP) Bond Lengths and Angles for RuS, $RuSO_2$, and $RuSO_2$/SO[a]

	RuS	$RuSO_2$	$RuSO_2$/SO
Ru−S(1), Å	2.2942 (2.2900)	2.3143 (2.3102)	2.3714 (2.3622)
Ru−S(2), Å	2.4088 (2.4057)	2.2508 (2.2473)	2.2592 (2.2548)
Ru−S(3), Å	2.3824 (2.3754)	2.4000 (2.3943)	2.3517 (2.3493)
Ru−P, Å	2.2973 (2.2911)	2.3529 (2.3519)	2.3906 (2.3790)
Ru−N(1), Å	2.2011 (2.198)	2.1999 (2.1927)	2.1821 (2.178)
Ru−N(2), Å	2.1936 (2.178)	2.1837 (2.200)	2.1974 (2.192)
P−Ru−S(2), deg	93.8 (95.4)	93.2 (93.2)	89.9 (90.7)
P−Ru−S(3), deg	92.1 (92.4)	92.4 (94.0)	93.1 (91.6)
S(2)−Ru−S(3), deg	94.5 (94.9)	95.4 (97.1)	94.8 (94.1)

[a]The experimental values are given in parentheses. S(1), thioether; S(2), thiolate/sulfinate; S(3), thiolate/sulfenate; N(1), axial nitrogen; N(2), equatorial nitrogen.

derived (X-ray crystal structure) data for RuS, $RuSO_2$, and $RuSO_2$/SO. As can be seen, there is excellent agreement between the calculated and experimental data, with the largest deviation in metal−ligand bond length being a 0.02 Å underestimation of the axial Ru−N bond in $RuSO_2$/SO. Most noteworthy is that the systematic elongation of the Ru−P bond upon thiolate oxygenation is reproduced; the B(38HF)-P86/TZVPP calculations show an increase from 2.30 Å in RuS (2.29 Å derived from crystallography) to 2.35 Å in $RuSO_2$ (2.35 Å derived crystallographically) to 2.39 in Å $RuSO_2$/SO (2.38 Å derived crystallographically). Thus, from a structural standpoint, this functional appears to reproduce the key metric parameters of these complexes effectively. It is worth noting that the B(38HF)P86 hybrid functional outperforms the more cost-effective BP86/VWN5 pure density functional, which overestimated the Ru−ligand bond lengths by as much as 0.2 Å (Supporting Information).

X-Ray Absorption Spectroscopy. *Ruthenium L-Edge X-Ray Absorption Spectroscopy.* The three ruthenium complexes RuS, $RuSO_2$, and $RuSO_2$ /SO were subjected to Ru L-edge X-ray absorption spectroscopy (Figure 2). These spectra

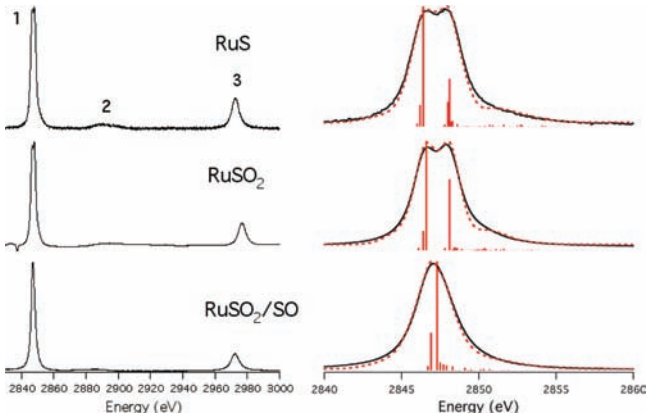

Figure 2. Ruthenium L-edge spectra for RuS (top), $RuSO_2$ (middle), and $RuSO_2$/SO (bottom). The left spectra are the full L_2/L_3 edge spectra. The transition marked 1 is the main L_3 transition. The features marked 2 result from nonbound transitions, and the transition marked 3 is the L_2 transition. The right depicts the main L_3 transitions. The experimental data are in black. The simulated spectra are the dashed red lines, and the individual transitions are the red sticks.

can be divided into essentially three regions. Region 1, the L_3 edge, results from Ru($2p_{3/2}$→ 4d) transitions. Higher in energy is region 2, which results from nonbound transitions originating from the Ru($2p_{3/2}$) ground state (e.g., EXAFS transitions). Finally, region 3, the L_2 edge, results from Ru($2p_{1/2}$→ 4d) transitions.

The Ru L-edge spectra of ruthenium-containing complexes cannot be adequately reproduced using single electron methods, indicating that multiplet effects are important for second-row transition metal L-edge spectroscopy.[71] Of the available approaches, there are two that have proven useful in simulating such spectra: *ab initio* TD-DFT-ZORA methods[71] and semiempirical approaches epitomized by the TT-multiplets/CT4XAS programs.[43,49] The simulations of the L-edge spectra presented herein utilize the latter approach, as it is one of the only general approaches available that considers atomic multiplets, crystal-field effects, and charge transfer effects in the simulation of L-edge data.[49] Furthermore, the simulation parameters are easily interpretable in terms of both crystal-field and covalency parameters, which are chemically intuitive and can be difficult to extract from the TD-DFT methods available.

These simulations start by calculating the atomic spectrum and extending the atomic Hamiltonian by including crystal-field effects. We consider the complexes to be nominal C_4 symmetric; thus the simulations include the crystal field energies $10D_q$, D_s, and D_t. Additionally, charge transfer effects were included in the simulations within a valence bond configuration interaction (VBCI) model. The VBCI model requires additional parameters for transfer integrals (T_{B_1}, T_{A_1}, T_{B_2}, and T_E), which describe Ru−ligand covalent overlap, and the energies for the separation between normal and charge transfer states in the ground and final states (Δ and Δ_f; see the Experimental Section).[75−77] The VBCI model is required for systems that have a high degree of covalency; in such systems, the ground and excited state wave functions must be extended to account for their multiconfigurational nature.[74] Although the use of the VBCI model is atypical for non-first-row transition metal compounds, we found that it was required to best fit the data for these more covalent Ru complexes (i.e., RuS and

dx.doi.org/10.1021/ic202453c | Inorg. Chem. 2012, 51, 6032−6045

$RuSO_2$, *vide infra*). For completeness, we also used the VBCI model to simulate the Ru L-edge spectrum of $RuSO_2$/SO, but note that the spectrum could be adequately reproduced within a simple atomic/crystal-field multiplets model (Supporting Information). Simulations of the spectra are accomplished by modeling the individual transitions as pseudo-Voigt line-shapes (1.15 eV line broadening). All of these parameters are systematically varied until a best fit to the data.

The atomic Hamiltonians for the three complexes are thus constructed for Ru^{2+}. It was necessary to include a reduction in Slater−Condon integrals to 80% of their atomic values to partially account for covalency. The atomic Hamiltonians used for simulating the L-edge spectra were further expanded using a crystal field model. This gives our first insight into the differential nature of the bonding of the three complexes. The crystal-field terms describing the energies of the Ru(4d) orbitals decrease across the series as the complexes are sequentially oxygenated (Table 2; Supporting Information). For example,

Table 2. Ru L-Edge Data and Simulation Parameters for RuS, $RuSO_2$, $RuSO_2$/SO

	RuS	$RuSO_2$	$RuSO_2$/SO
L_3 maximum (eV)	2846.4/2847.8	2846.8/2849.0	2847.1
L_2 maximum (eV)	2972.9	2973.2	2972.4
branching ratio[a]	0.81	0.76	0.71
$10D_q$ (eV)	3.81	3.64	3.58
D_t (eV)	0.21	0.18	0.40
D_s (eV)	0.10	0.15	0.00
$\Delta_{a_1/b_1}(eV)$[c]	1.34	1.47	1.60
Δ (eV)	2.8	2.6	2.9
Δ_f (eV)	0.6	0.8	1.1
T_{B_1} (eV)	1.9	1.4	0.3
T_{A_1} (eV)	1.1	0.6	0.0
T_E (eV)	1.0	0.4	0.2
T_{B_2} (eV)	0.2	0.2	0.0
$\|4d^6\rangle$[b]	0.79	0.84	0.99

[a] $I_3/(I_3 + I_2)$. [b] Fraction of $|4d^6\rangle$ character in the ground-state wave function. [c] The energy difference between the a_1 and b_1 states.

$10D_q$ decreases across the series from 3.81 eV in RuS to 3.64 eV in $RuSO_2$ to 3.58 eV in $RuSO_2$/SO. This suggests that there is less of a bonding interaction between the ligands and the Ru(II) center as the complexes become sequentially oxygenated. Such a supposition is fully supported by the VBCI model.

Because of the high degree of Ru−ligand covalency, we need to consider the ground wave functions as being linear combinations of the normal $|4d^6\rangle$ and charge transfer $|4d^7\underline{L}\rangle$ states. Thus, the excited state wave functions are also linear combinations of the $|\underline{2p}4d^7\rangle$ and charge transfer $|\underline{2p}4d^8\underline{L}\rangle$ states (see Experimental Section). Such a situation is most easily accounted for within the VBCI model described above. It is of note that the values obtained for Δ_f (Table 2), which represents the difference in energy between the $|\underline{2p}4d^7\rangle$and $|\underline{2p}4d^8\underline{L}\rangle$ states, are only slightly reduced from those obtained from investigations of first-row transition metal complexes.[72] This suggests that the reduction in 2p/4d Coulombic attraction is mostly offset by a reduction in 4d/4d Coulombic repulsion, owing to the more diffuse nature of the 4d vs 3d orbitals.

As suggested by the crystal-field parameters, the VBCI analysis shows that the covalency of the Ru−ligand bonds significantly decreases as the Ru compounds become oxygenated. This is demonstrated by the magnitude of the transfer integrals T; the larger the value of T, the more ligand character there is in a particular configuration. All of the transfer integrals decrease significantly upon oxygenation, suggesting a decrease in covalency (Table 2). Most striking is the reduction in the T_{A_1} and T_E transfer integrals. The T_E transfer integral is reduced from 1.0 eV for RuS, to 0.4 eV for $RuSO_2$, and to 0.2 eV for $RuSO_2$/SO. Similarly, the T_{A_1} transfer integral is reduced from 1.1 for RuS, to 0.6 eV for $RuSO_2$, and to 0.0 eV for $RuSO_2$/SO. Thus, there is a marked reduction in covalency to the $Ru(4d_{z^2})$ and to the $Ru(4d_{xz/yz})$ orbitals upon oxygenation of the complexes. In fact, all of the transfer integrals for the most oxygenated complex $RuSO_2$/SO are suggestive of a compound with significantly diminished covalent character compared with the other two Ru complexes investigated.

The reduction in covalency to the $Ru(4d_{xz/yz})$ is easily rationalized. In the unoxygenated complex, this orbital set is predominantly $S(\pi)$−$Ru(\pi)$ in character. Upon oxygen atom insertion, these $S(\pi)$ orbitals are now involved in S−O bonding and leave these orbitals unavailable for bonding to the $Ru(4d_{xz/yz})$ orbitals. The reduction in covalency to the $Ru(4d_{z^2})$ orbital is less easily rationalized as the $S(\sigma)$ interactions would be not as strongly affected upon oxygen atom insertion and may be a result of differential covalency along the molecular z axis (i.e., axial amine or phosphine coordination).

An additional feature of note pertinent to the Ru L-edge spectra is the branching ratio, which is defined as

$$\text{branching ratio} = \frac{I_3}{(I_2 + I_3)} \tag{9}$$

where I_3 and I_2 are the integrated intensities of the Ru-L_3 and the Ru-L_2 edges, respectively.[79] For the three complexes investigated, we find a systematic decrease in the branching ratio as the compounds are oxygenated; it decreases from 0.81 in RuS to 0.76 in $RuSO_2$ to 0.71 in $RuSO_2$/SO (Table 2). It has been shown that two factors influence the branching ratio: metal complex spin state and oxidation state.[80,81] For example, in nickel complexes, it has been noted that as the oxidation state is decreased the branching ratio increases.[81] Also, as the spin-state increases so does the branching ratio. The three ruthenium complexes studied are all low spin, suggesting that there should be a minimal change in branching ratios on this basis. However, if we consider the multiconfigurational nature of the ground states, the trend in branching ratios can be rationalized. The most covalent compound, RuS, has the highest degree of Ru(I) character (i.e., $Ru(4d^8\underline{L})$ composition) in the ground-state wave function (21%, Table 2). The amount of Ru(I) character decreases to 16% in $RuSO_2$ and 1% in $RuSO_2$/SO. The branching ratios are thus consistent with the decreasing degree of charge-transfer character in the ground state wave functions of these compounds as the complexes are sequentially oxygenated.

Sulfur K-Edge X-Ray Absorption Spectroscopy. It has been well established that ligand K-edge spectroscopy can be used as a direct probe of ligand−metal covalency in transition metal complexes.[82] In S K-edge spectroscopy, the main absorption feature is attributed to the $S(1s) \rightarrow S(3p)$ transition. However, in the case of transition metal complexes containing covalent S−M bonds, the pre-edge region of the S K-edge spectrum contains intense transitions into other lower-energy states. These transitions gain intensity through a mixing of

dx.doi.org/10.1021/ic202453c | Inorg. Chem. 2012, 51, 6032−6045

S(3p) character into the acceptor states, which makes the transitions electronic dipole allowed.[82−85]

In S K-edge XAS, the normalized transition intensity of the pre-edge peak, $Int_{1s\rightarrow\Psi^*}$, is given by

$$Int_{1s\rightarrow\Psi^*} = \alpha^2|\langle S(1s)|\hat{e}\cdot r|\Psi^*\rangle|^2 = \frac{A}{3n}\alpha^2 I_S \quad (10)$$

where n is a normalization factor accounting for the number of sulfur atoms contributing to the transition, A is the ground state degeneracy, I_S is the transition dipole integral of the metal bound sulfur atom, and Ψ^* is the normalized acceptor wave function.[87] For example, for a S(1s) → "Ru(4d)" transition, Ψ^* would be

$$\Psi^* = (1 - \alpha^2)^{1/2}|Ru(4d)\rangle - \alpha|S(3p)\rangle \quad (11)$$

where α^2 is the degree of S(3p) character in Ψ^*. By comparison of the intensity of these pre-edge features to thiolate-ligated transition metal complexes with known S(3p) character and I_S, one can obtain the S covalency of the investigated compound.

The pre-edge region of the S K-edge X-ray absorption spectra for the three complexes probed are depicted in Figure 3.

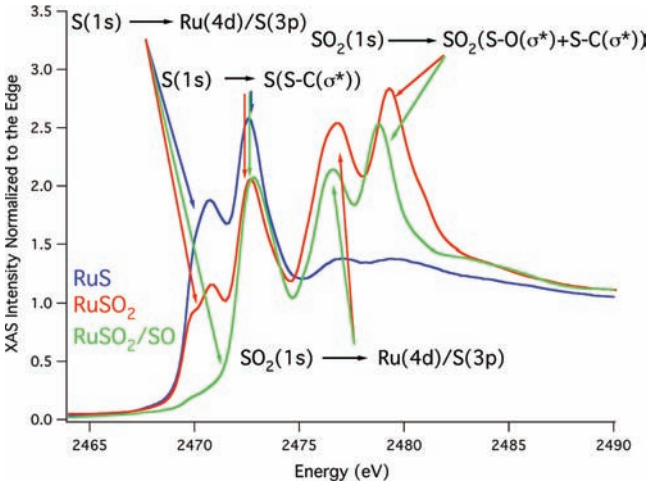

Figure 3. Sulfur K-edge spectra of RuS (blue), $RuSO_2$ (red), and $RuSO_2$/SO (green). The SO-based transitions for $RuSO_2$/SO are buried under the S(1s) → S−C(σ^*) and SO_2(1s) → Ru(4d)/S(3p) transitions and are therefore not highlighted.

In order to best compare the differences between the spectra, we will examine the individual features of the three spectra in order of energies. On the basis of previous S K-edge studies, we can assign the features in the S K-edge spectra as follows.[48,91] The initial transitions encountered at ∼2471 eV correspond to transitions from the S(1s) AO to the Ru(4d)/S(3p) manifold followed by transitions from the S(1s) AO to the ligand S(S−C(σ^*)) orbitals at ∼2−3 eV higher in energy. Next come the SO(1s) → Ru(4d)/S(3p) and S(1s) → SO(S−O(σ^*)/S−C(σ^*)) transitions at ∼2474 and ∼2478 eV, respectively. Highest in energy are the SO_2(1s) → Ru(4d)/S(3p) and SO_2(1s) → SO_2(S−O(σ^*)+S−C(σ^*)) transitions at ∼2476 and ∼2480 eV, respectively.

S(1s) → Ru(4d)/S(3p) Transitions. The spectra of both RuS and $RuSO_2$ display prominent low energy features at ∼2471 eV, which correspond to nominal thiolate based S(1s) → Ru(4d)/S(3p) transitions. It is apparent that the intensity of this transition in RuS is approximately double the intensity for $RuSO_2$, which reflects the conversion of one of the two thiolate ligands into a sulfinate ligand. Thus, the number of thiolate S(1s) electrons in RuS is double that in $RuSO_2$. In each compound, the pre-edge feature displays significant asymmetry. This reflects transitions into the two available Ru(4d)/S(3p) MOs, which can be readily deconvolved in the data analysis. In nominal C_4 symmetry, these correspond to S(1s) transitions into the a_1 and b_1 states. These transition assignments are based on both the analysis of the of the Ru L-edge data and from the electronic structure calculations performed on the three complexes (see section Bonding Description and Löwdin Population Analysis). We note that the degree of splitting observed for these two transitions (∼1.1 eV), although smaller, are consistent with the calculated ligand field diagrams derived from the Ru L-edge simulations (Table 2). The integrated intensity of the two transitions for RuS yield total %S(3p) contributions to the a_1 and b_1 states of 26% and 61%, respectively ($E_{S(1s)\rightarrow a_1}$ = 2471.0(1) eV, $E_{S(1s)\rightarrow b_1}$ = 2472.1(1) eV; see Table 2). Upon the oxidation of RuS to $RuSO_2$, the covalency of the a_1 and b_1 states are altered to 38% and 56%, respectively ($E_{S(1s)\rightarrow a_1}$ = 2470.9(1) eV, $E_{S(1s)\rightarrow b_1}$ = 2472.0(1) eV). *Thus, the reduction in covalency of the a_1 state of RuS vs $RuSO_2$ observed in the analysis of the Ru L-edge data of RuS vs $RuSO_2$ is not the result of reduced S character as the overall S covalency remains essentially constant in Ru_2 vs $RuSO_2$.* A similar compensatory effect was noticed in systematically oxygenated NHase model compounds in studies by Kovacs and Solomon; in bis-thiolate ligated NHase models, it is observed that as one of the thiolates is oxygenated the unmodified Fe−thiolate bond becomes significantly more covalent than before.[16,17]

For $RuSO_2$/SO, a small band resulting from the thioether S(1s) → Ru(4d)/S(3p) transition is observed and can be deconvolved from the edge. Compared with the thiolate-based S(1s) → Ru(4d)/S(3p) transitions observed for both RuS and $RuSO_2$, there is a slight red-shift in energy of the thioether-based transition from $RuSO_2$/SO (to 2472.5(8) eV). Integration of this feature results in 38(8)% *combined* %S(3p) character for both the a_1 and b_1 states. The large uncertainty in the derived thioether S-covalency parameter is the result of difficulty in reliably extracting the intensity of the peak from the experimental $RuSO_2$/SO S K-edge data. We also note that in the case of both RuS and $RuSO_2$ the thioether transition is obscured by the thiolate-based and edge transitions. The above derived %S(3p) compositions of the a_1 and b_1 states for RuS and $RuSO_2$ may therefore be slightly overestimated.

S(1s) → S(S−C(σ^*)) and SO(1s) → Ru(4d)/S(3p) Transitions. Higher in energy, one observes the S(1s) → S(S−C(σ^*)) transitions at ∼2473.5 eV. There is a reduction in intensity of this transition upon oxygenation of the RuS to $RuSO_2$, which is a direct result of the conversion of a thiolate to a sulfinate. Upon conversion of the thiolate in $RuSO_2$ to a sulfenate in $RuSO_2$/SO, this peak intensity remains virtually unchanged. We attribute this to an overlapping SO(1s) → Ru(4d)/S(3p) transition. An intense band can be deconvolved from the S K-edge data for $RuSO_2$/SO (see Supporting Information Figure S-4) that corresponds to an appropriate energy for the SO(1s) → Ru(4d)/S(3p) transition (∼ 2474.2 eV) based on previous experiments.[91] However, considering the uncertainty in its energy/intensity, we cannot reliably extract covalency parameters for this transition.

SO_2(1s) → Ru(4d)/S(3p) and SO_2(1s) → SO_2(S−O(σ^*) + S−C(σ^*)) Transitions. Well resolved from the S(1s) → S(S−C(σ^*)) transition in both $RuSO_2$ and $RuSO_2$/SO is the

dx.doi.org/10.1021/ic202453c | *Inorg. Chem.* 2012, 51, 6032−6045

$SO_2(1s) \rightarrow Ru(4d)/(3p)$ transition. Previous studies by Solomon and co-workers demonstrate that I_S is modulated by the charge on the S atom; as the charge on S becomes more positive, I_S increases.[48,88−90] This increase in I_S was found to correspond linearly with the increase in the energy of the S(1s) $\rightarrow \Psi^*$ transition. Using previously determined values for I_S as a function of energy, we derive a value for I_S of 18.1 for the $SO_2(1s) \rightarrow$ LUMO transitions of both $RuSO_2$ and $RuSO_2$/SO ($E_{SO_2(1s)} \rightarrow a_1$ = 2476.0 eV). Curiously, the %S(3p) character in the a_1 and b_1 states for the $RuSO_2$ based $SO_2(1s) \rightarrow$ S(3p) transitions are comparable with those observed for the thiolate based S(1s) $\rightarrow$ S(3p) transitions, suggesting comparable covalencies. We determine that the a_1 state contains 39% S(3p) character, while the b_1 state contains 56% S(3p) character. For $RuSO_2$/SO, the derived %S(3p) characters to the a_1 and b_1 states are reduced to 57% *combined* (Table 2) and thus represent a dramatic reduction in S covalency upon sulfinate/sulfenate formation. Slight inconsistencies in the individual refinements make splitting this into the individual a_1 and b_1 contributions tenuous. The last prominent features in the $RuSO_2$ and $RuSO_2$/SO S K-edge spectra are the SO_2 (1s) $\rightarrow$ SO_2 (S−Oσ^* + S−Cσ^*) transitions, which occur at ∼2480 eV.

It should be re-emphasized that the SO_2 (1s) $\rightarrow$ S(3p) transitions may overestimate the %S(3p) character to the a_1 and b_1 acceptor states.[92] For $RuSO_2$, the %S(3p) character derived for the $SO_2(1s) \rightarrow$ S(3p) transition may be overestimated due to baseline irregularities (i.e., oscillations due to XANES effects). The %S(3p) character derived for the $SO_2(1s) \rightarrow$ S(3p) transition for $RuSO_2$/SO may be overestimated due to the overlapping SO $\rightarrow$ SO(S−Oσ^* + S−Cσ^*) transition. Care has been taken to account for this overlapping transition in the spectral deconvolution (see Supporting Information; Figures S4) where the likely SO $\rightarrow$ SO(S−Oσ^* + S−Cσ^*) transition was observed. However, we cannot ensure that the covalency parameters obtained for $RuSO_2$/SO have not been overestimated. Therefore, the %S(3p) values reported for the Ru−SO_2 bond in Table 3 should be viewed as upper limits.

Nitrogen K-Edge X-Ray Absorption Spectroscopy. In an analogous manner to S K-edge XAS, it should be possible to extract covalency parameters for light-atom transition metal bonds using X-ray absorption methods. There have been few reports in the literature where the light-atom ligands (e.g., O and N derived ligands) of transition metal complexes have been investigated by XAS techniques.[93,94] Of these limited studies, we are not aware of any XAS studies in which transition metal−ligand covalency parameters have been extracted for these light atoms. This is undoubtedly because of the difficulties inherent in obtaining reproducible/interpretable data for these low energy transitions (e.g., ultrahigh vacuum techniques, sample preparation/contamination issues, saturation effects, etc.) coupled with the fact that transition-metal nitrogen bonds do not display high degrees of covalency. Thus, we have chosen to investigate RuS, $RuSO_2$, and $RuSO_2$/SO by N K-edge XAS to (a) provide a small basis set of compounds with known covalency/I_N parameters and (b) explore the bonding in these complexes by probing beyond the S and Ru centers.

The experimental spectra for RuS, $RuSO_2$, and $RuSO_2$/SO are displayed in Figure 4a. All three spectra display a sharp pre-edge feature followed by the onset of the edge transitions. To better understand the origin of the features in the pre-edge region of the N K-edge X-ray absorption spectra, time-dependent density functional theory (TD-DFT) calculations were undertaken using the geometry optimized structures described above. These calculations involved the use of Neese's triple-ζ segmented all-electron relativistic basis set (def2-TZVP(-f)),[60,61] the B3LYP hybrid functional,[62−65] and the scalar relativistic zeroth-order approximation (ZORA).[69,70] Use of the ZORA had a minimal influence on the resulting simulated spectra, as may be expected because the spectra of second row elements were simulated.[95] As good agreement with the experimental data was obtained employing the B3LYP functional, more costly computational methods were not explored.

Figure 4b−d displays the simulated N K-edge spectra for RuS, $RuSO_2$, and $RuSO_2$/SO. These were produced by red-shifting all transitions by 20.5 eV, followed by applying a Gaussian line shape to the individual transitions (0.75 eV peak-width at half-height) and summing the individual Gaussian line shapes. These simulations produced a well resolved pre-edge feature that corresponded to the N(1s) $\rightarrow$ LUMO transition (i.e., N(1s) $\rightarrow a_1$). As can be seen from Figure 4c and d, most of the intensity of this transition results from the promotion of a N(1s) electron originating from the axial nitrogen. Thus, the intensity of this transition is a direct reflection of the degree of axial nitrogen character in the LUMO. This is also observed in the Löwdin population analysis (*vide infra*). The calculations also suggest that the energies of the N(1s) $\rightarrow b_1$ transitions range from 0.9 to 1.5 eV higher in energy than the N(1s) $\rightarrow a_1$ transition and would thus be buried in the edge of both the simulated and experimental spectra. We note that the magnitude of the splitting in the a_1 and b_1 states derived from the TD-DFT simulations of the N K-edge spectra are

Table 3. Analysis of the Pre-Edge Region of the S K-Edge Spectra of RuS, $RuSO_2$, and $RuSO_2$/SO

	RuS	$RuSO_2$	$RuSO_2$/SO
	S(1s) → Ru(a_1)		
energy (eV)	2471.0(1)	2470.9(1)	
area (% eV rel. to edge)	70.1(3)	50.4(3)	
$\%S_{3p}$	26.4(4)%	38.0(4)%	
	S(1s) → Ru(b_1)		
energy (eV)	2472.1(1) eV	2472.0(1)	
area (% eV rel. to edge)	162(1)	73.8(3)	
$\%S_{3p}$	61.1(3)%	55.6(4)%	
	$S_{thioether}$(1s) → Ru(4d)		
energy (eV)			2472.5(8)
area (% eV rel. to edge)			44(5)
$\%S_{3p}$			38(8)%
	$SO_2(1s) \rightarrow Ru(a_1)$		
energy (eV)		2475.9(3)	2476.1(4)[a]
area (% eV rel. to edge)		117(1)	77(1)
$\%S_{3p}$		39(1)%	26(1)%
	$SO_2(1s) \rightarrow Ru(b_1)$		
energy (eV)		2476.9(3)	2476.9(3)[a]
area (% eV rel. to edge)		170(3)	94(1)
$\%S_{3p}$		56(1)%	31(1)%
	S(1s) → C−S(σ^*)		
energy (eV)	2473.6(1)	2473.7(1)	2473.7(1)
	$SO_2(1s) \rightarrow$ C−S(σ^*) + O−S(σ^*)		
energy (eV)		2480.1(1)	2479.4(1)

[a]In the text these are represented as 57% combined. The results reported here come from the two peaks corresponding to these transitions from the deconvolved spectrum.

dx.doi.org/10.1021/ic202453c | *Inorg. Chem.* 2012, 51, 6032−6045

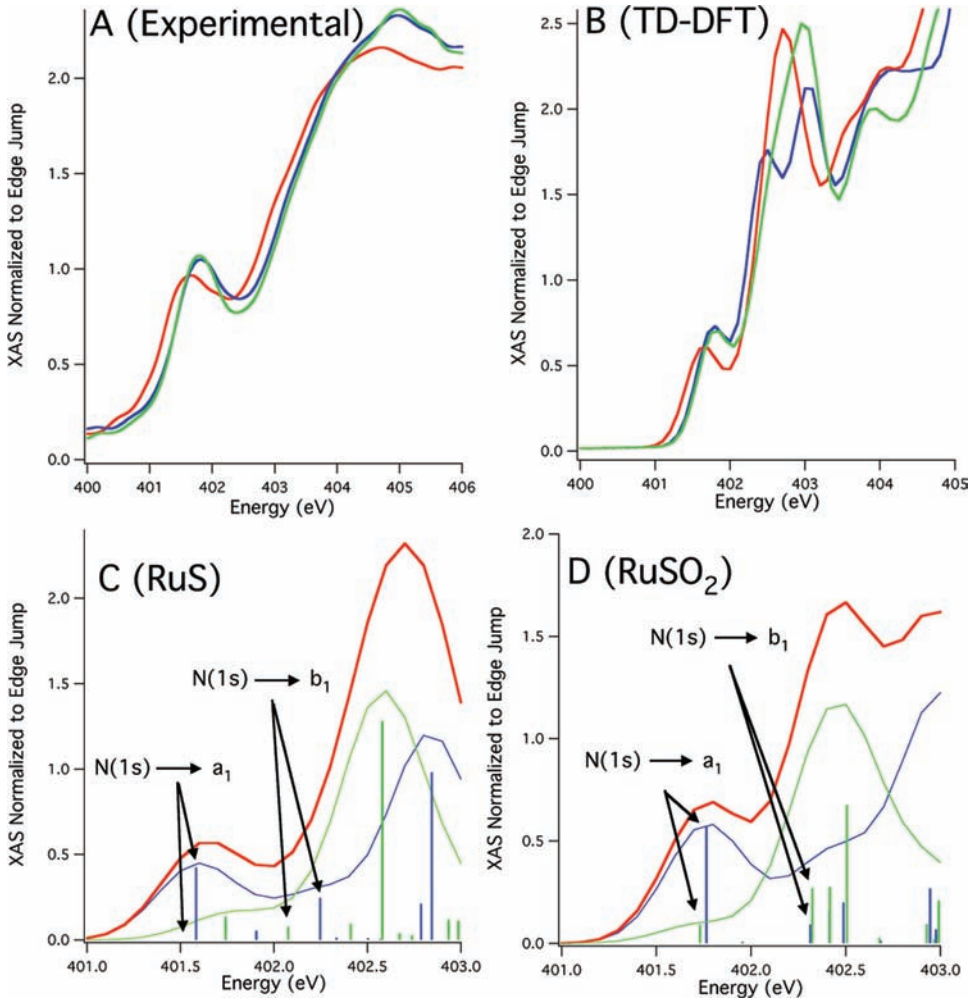

Figure 4. (A) Experimental N K-edge spectra of RuS (red), $RuSO_2$ (blue), and $RuSO_2$/SO (green). (B) Simulated N K-edge spectra for RuS (red), $RuSO_2$ (blue), and $RuSO_2$/SO (green) using TD-DFT (B3LYP/def2-TZVP(-f)). (C) Simulated pre-edge region of the N K-edge X-ray absorption spectrum of RuS (red) deconvolved into contributions from the axial (blue) and equatorial (green) nitrogen atoms. (D) Simulated pre-edge region of the N K-edge X-ray absorption spectrum of $RuSO_2$ (red) deconvolved into contributions from the axial (blue) and equatorial (green) nitrogen atoms.

consistent with both the S K-edge and Ru L-edge experimental data (Tables 2 and 3).

Turning back to the experimental spectra (Figure 4a), based on TD-DFT calculations, we can attribute this resolved pre-edge feature to the N(1s) → LUMO transition (i.e., transition into the a_1 state). Using eq 10, we can determine the degree of N(2p) character corresponding to the LUMO by determining a value for I_N. In a previous study, we utilized Ni L-edge and S K-edge XAS coupled with high-level computational methods to derive a description of the ground state wave function for the bis-amine bis-thiolate $Ni^{II}N_2S_2$ complex (bmmp-dmed)Ni. From these data, we determined that the %N(2p) character in the LUMO was 6.8(2)%. In this study, we measured the N K-edge spectrum of (bmmp-dmed)Ni (Supporting Information, Figure S-1) and determined that the peak area of the N K-edge pre-edge feature is 42.6(2)% eV relative to the edge jump. This corresponds to 15.6(2)% N(2p) character per 100(1)% eV relative to the edge jump per N atom using our deconvolution scheme. This translates into an I_N = 38.5(4) at 401.7 eV. Although this value may seem large when compared to the S K-edge data, it is consistent with the less diffuse nature of the N(2p) orbitals in comparison to the S(3p) orbitals.[96]

Unlike the systematic decrease in the Ru−S covalency observed upon progressive thiolate oxygenation, the N K-edge data indicate a small but systematic *increase* in the N(2p) character to the a_1-type state upon sequential thiolate oxygenation. For RuS, the experimentally determined % N(2p) character to the LUMO is 4%. This value increases to 5% and 6% for $RuSO_2$ and $RuSO_2$/SO, respectively (Table 4).

Table 4. Results from the Analysis of the Pre-Edge Region of the N K-Edge Spectra of RuS, $RuSO_2$, and $RuSO_2$/SO

	RuS	$RuSO_2$	$RuSO_2$/SO
energy (eV)	401.6(1)	401.7(1)	401.7(1)
area (% eV rel. to edge)	28.2(2)%	33.4(2)%	39.1(1)%
$\%N_{2p}$	4.4(2)%	5.2(2)%	6.1(2)%

A similar trend is observed in the simulated TD-DFT N K-edge spectra where a small but systematic increase in oscillator strength is predicted upon sequential oxygenation of the thiolate sulfurs. As stated, TD-DFT calculations demonstrate that the N(1s) → b_1 transition is buried in the edge region of the spectra (Figure 4). Therefore, we cannot extract the nitrogen composition to the b_1 states in these complexes from

dx.doi.org/10.1021/ic202453c | *Inorg. Chem.* 2012, 51, 6032−6045

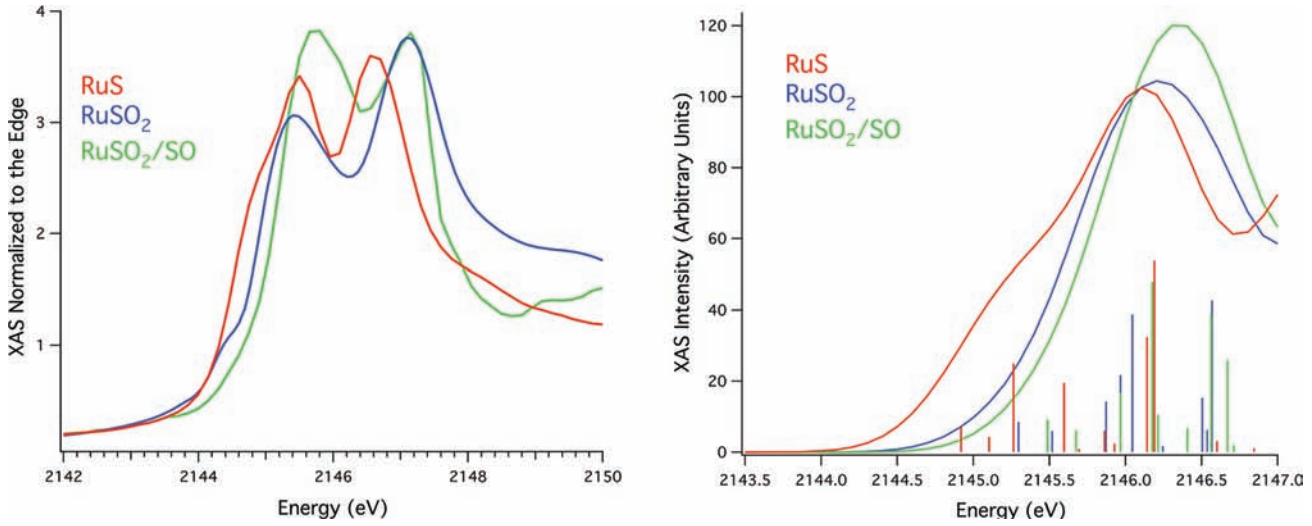

Figure 5. (Left series of spectra) The experimental phosphorus K-edge spectra of RuS (red), $RuSO_2$ (blue), and $RuSO_2$/SO (green). (Right series of spectra) The simulated phosphorus K-edge spectra for RuS (red), $RuSO_2$ (blue), and $RuSO_2$/SO (green) using TD-DFT (B3LYP/def2-TZVP(-f)). Individual transitions are given as sticks. To simulate the spectra, a 1.0 eV line width was applied to all transitions.

the N K-edge data. *However, both the experimental data and the TD-DFT simulations show that as the thiolate sulfur atoms are oxygenated the degree of nitrogen covalency to the LUMO increases.*

Phosphorus K-Edge X-Ray Absorption Spectroscopy. The P K-edge X-ray absorption spectra for RuS, $RuSO_2$, and $RuSO_2$/SO are depicted in Figure 5. These spectra all resemble the P K-edge spectrum of PPh_3, but with some notable differences.[42] The P K-edge spectrum for PPh_3 displays two sharp transitions in the pre-edge region at 2145.7 and 2147.6 eV corresponding to low-lying P(1s) → P(P−C(π*)) transitions.[42] In the three Ru(II) complexes studied, the lower energy transition displays significant broadening and asymmetry compared to PPh_3. Furthermore, relative to PPh_3 the peak maxima also shift to a lower-energy for both the RuS and $RuSO_2$ complexes, while it is higher in energy relative to PPh_3 for the $RuSO_2$/SO complex (Table 5). For the three complexes investigated, there is a systematic increase in intensity of this pre-edge feature upon oxygenation, suggesting a larger contribution of P-atomic character in the wave functions of these acceptor states.

Table 5. Results from the Analysis of the Pre-Edge Region of the P K-Edge Spectra of RuS, $RuSO_2$, and $RuSO_2$/SO

	RuS	$RuSO_2$	$RuSO_2$/SO
	peak 1		
energy (eV)	2144.8(2)	2144.4(2)	2144.6(4)
area (% eV rel. to edge)	62.2(2)%	31.9(6)%	9(1)%
	peak 2		
energy (eV)	2145.5(1)	2145.4(1)	2145.8(1)
area (% eV rel. to edge)	122(1)%	208(2)%	287(2)%
	peak 3		
energy (eV)	2146.7(1)	2147.6(1)	2147.6(1)
area (% eV rel. to edge)	243(2)%	246(2)%	251(3)%

There are several reasons why an extensive analysis of the P K-edge spectrum for the three complexes probed was not undertaken. One is that there is no well-defined standard where I_P has been determined. Thus, Ru−P covalency parameters cannot be reliably extracted. Furthermore, there is significant band overlap making spectral deconvolutions unreliable. As can be seen from the TD-DFT results of the P K-edge simulations depicted in Figure 5, there are a large number of excited states which are close in energy to one another. Thus, the degree of P(3p) character in these wave functions cannot be determined spectroscopically with any degree of accuracy from these data. However, the asymmetry of the first band of the P K-edge spectra of the complexes can be rationalized in light of excited-state calculations.

Figure 5 displays the simulated P K-edge spectra of RuS, $RuSO_2$, and $RuSO_2$/SO. These were simulated in a manner similar to the N K-edge spectra, but with a 26.3 eV red shift applied to the transitions and a 1.0 eV line-width applied to the transitions. As can be seen, a reasonable match in the shapes and intensities of the experimental vs calculated data is achieved. The lowest energy transitions in the P K-edge spectra are due first to the P(1s) → LUMO transitions (e.g., the P(1s) → a_1 transitions from above), which are low intensity transitions relative to the slightly higher energy ligand-based P(1s) → P(C−P(π)) transitions. This P(1s) → LUMO transition can be observed in the experimental RuS P K-edge spectrum as the low-energy shoulder in the pre-edge region. Upon successive oxygenation of the thiolates, the intensity of this transition significantly decreases, demonstrating that the degree of P(3p)-character to the LUMO significantly decreases upon oxygenation as well. The experimental data coupled with simulations also demonstrate that upon oxygenation the transitions into the unfilled C−P(π)*-type states gain intensity, move to higher energy, and begin to better resemble the P K-edge X-ray absorption spectrum of free PPh_3. Taken together, the experimental and calculated P K-edge data seem to suggest that the phosphine ligand is more weakly coordinating to the Ru(II) center as the thiolates become more oxygenated.

Bonding Description and Löwdin Population Analysis. Single point calculations utilized the B(HF38)P86 functional and the large quadruple-ζ def2-QZVPP basis set. Figure 6 depicts the isosurface plots of the resulting MOs that are comprised of mostly 4d character and the energies of the HOMO−2 to LUMO+5/6 normalized to the energy of the HOMO. As can be seen, there are several low-lying unfilled orbitals of mostly ligand character that have energies between the Ru($4d_{z^2}$) (a_1) and the Ru($4d_{x^2-y^2}$) (b_1) MOs. These are a

dx.doi.org/10.1021/ic202453c | Inorg. Chem. 2012, 51, 6032−6045

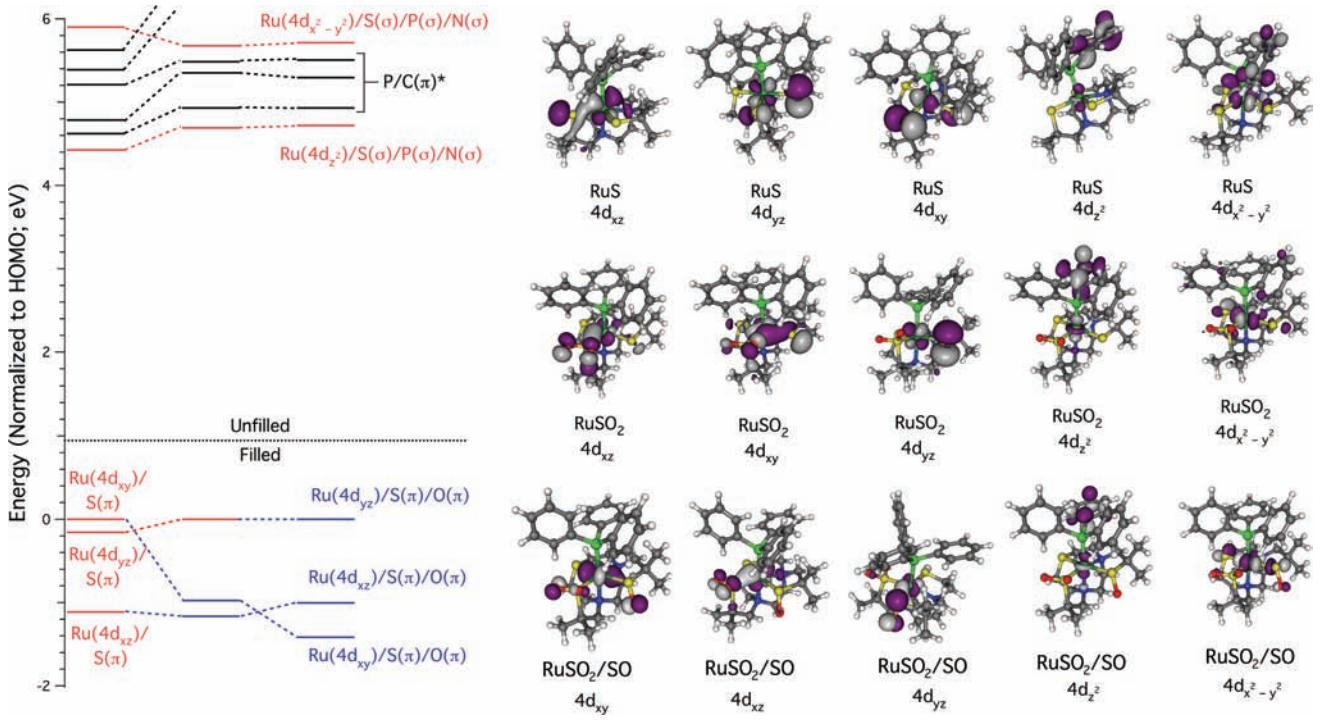

Figure 6. Left: The energy level diagram of the valence molecular orbitals that are predominately 4d in character obtained from the B(38HF)P86 hybrid density functional theory calculations (def2-QZVPP) of RuS (left), $RuSO_2$ (middle), and $RuSO_2$/SO (right). The orbitals in red contain no oxygen AO character. Those in blue contain Ru(4d) and oxygen AO character, while those in black are ligand based with no Ru character. All orbital energies have been normalized to the HOMO. Right: Isosurface plots of the valence molecular orbitals that are predominately 4d in character (RuS (top), $RuSO_2$ (middle), and $RuSO_2$/SO (bottom)).

result of P−C(π)* antibonding interactions localized on the triphenylphosphine ligand. Transitions into states comprised of these orbitals in the P K-edge spectra will dominate the P K-edge spectra of these complexes, as was observed (*vide supra*).

Table 6 displays the Löwdin population analysis[97] describing the atomic-orbital contributions of the ligating atoms and Ru that comprise the Ru(4d)-type MOs for RuS, $RuSO_2$, and $RuSO_2$/SO. The first observation is that there is good agreement between the calculated sulfur populations of the $4d_{z^2}$ and $4d_{x^2-y^2}$ MOs and the experimentally observed S(3p) contribution to the a_1 and b_1 states. Thus, the B(38HF)P86/def2-QZVPP hybrid functional and basis set appear to be capable of producing physically meaningful results for these Ru−thiolate complexes.

An overall decrease in S character in the corresponding wave functions is observed as the thiolate sulfurs become oxygenated. For the a_1 state, the experimental data correspond to a %S(3p) character of 26% and 38% for RuS and $RuSO_2$, while the calculated S character corresponds to 26% and 36% S character for RuS and $RuSO_2$. Similarly, for the b_1 state, the experimental data correspond to a %S(3p) character of 61% and 56% for RuS and $RuSO_2$, while the calculated S character obtained is 60% and 51% for RuS and $RuSO_2$. Direct comparison of the experimental and calculated %S(3p) character found in $RuSO_2$/SO is a bit more troublesome because of the spectral overlap found in the S K-edge spectrum of $RuSO_2$/SO. The experimental data indicate a range of 38−57% S(3p) for the a_1 and b_1 type orbitals combined. The computational data suggest that the %S(3p) to the a_1 state is 27.2% and to the b_1 state is 29.8% (57.0% combined). Considering the agreement between experimental and computationally derived data for the RuS and $RuSO_2$ complexes, we can assume that the %S(3p) character derived from the B(HF38)BP86/def2-QZVPP calculations for $RuSO_2$/SO are reasonably accurate. Thus, these results show that there is not a linear relationship

Table 6. Atomic Orbital Populations (as percentage) to the Resulting "Ru(4d)" Molecular Orbitals for RuS, $RuSO_2$, and $RuSO_2$/SO (Löwdin Population Analysis: B(HF38)P86/QZVPP)[a]

	S(1)	S(2)	S(3)	P	N(1)	N(2)	Ru
			HOMO-2				
RuS	0.6	0.7	27.1	4.9	0.0	3.7	47.2
$RuSO_2$	2.6	5.8	13.0	1.1	0.1	2.6	41.9
$RuSO_2$/SO	3.0	4.1	11.9	0.8	0.1	2.2	40.3
			HOMO-1				
RuS	0.6	47.0	11.0	0.9	0.4	0.0	22.1
$RuSO_2$	4.8	25.5	5.3	0.5	0.2	0.9	33.9
$RuSO_2$/SO	11.2	6.3	4.7	0.5	0.2	1.4	36.6
			HOMO				
RuS	3.2	16.1	38.5	0.3	0.2	0.1	27.0
$RuSO_2$	1.4	58.2	0.1	1.4	0.5	0.0	18.9
$RuSO_2$/SO	1.4	9.1	0.1	1.7	1.8	0.1	30.0
			LUMO				
RuS	11.7	7.3	6.6	10.4	4.8	1.8	23.0
$RuSO_2$	18.8	17.6	0.3	7.4	6.1	1.9	32.1
$RuSO_2$/SO	21.4	4.2	1.6	0.3	7.2	1.8	39.8
			LUMO+4[b]				
RuS	2.3	28.3	30.2	13.8	1.5	0.7	25.1
$RuSO_2$	6.9	42.8	1.0	6.1	3.4	0.9	31.6
$RuSO_2$/SO	19.7	6.2	3.9	4.4	4.8	1.2	40.7

[a] S(1), thioether; S(2), thiolate/sulfinate; S(3), thiolate/sulfenate; N(1), axial nitrogen; N(2), equatorial nitrogen. [b] LUMO+6 for RuS.

dx.doi.org/10.1021/ic202453c | *Inorg. Chem.* 2012, 51, 6032−6045

between thiolate-oxygenation and the decrease in the %S(3p) character contained in these wave functions. This is because (a) the unoxygenated thiolate partially compensates for the lose of S character contribution from the oxygenated thiolate in $RuSO_2$ and (b) the thioether S becomes much more covalent as the thiolates are oxygenated in $RuSO_2$ and $RuSO_2$/SO. A similar effect has been noted by Solomon in computational/S K-edge work performed on some of Kovacs' NHase model compounds.[17]

The filled frontier orbitals for these Ru−thiolate complexes are dominated by Ru(4d(π))/S(π) interactions, with both thiolates extensively participating in antibonding interactions to the Ru(4d) orbitals. Little thioether character is observed in the HOMO through HOMO−2 for RuS. Upon oxygenation of RuS to $RuSO_2$, the S-contribution of the oxygenated thiolate is dramatically reduced as the S(π)-type AOs are now used for oxygen bonding. By analogy, the degree of covalency in the bonding MOs must also decrease. Despite this fact, the loss of the Ru(4d(π))/S(π) covalent interaction reduces the Ru−SO_2 bond length. This may seem counterintuitive, but its origin is well established. Upon oxygenation, the repulsive filled−filled interaction between the Ru(4d(π)) and the thiolate S(3p(π)) AOs are lost. This leads to a contraction of the Ru−SO_2 bond, as has been observed and rationalized before in oxygenated Ni−thiolate compounds, for example.[98] Another possible reason for the contraction of the Ru−SO_2 bond may be a contraction of the S(3p) AOs upon oxidation.

The S(3p(π)) AOs from the unmodified thiolate now dominate the HOMO wave function in $RuSO_2$ as it no longer competes with the now oxygenated thiolate. A similar, but not as dramatic, trend is also observed in HOMO−1 and HOMO−2. This is because the sulfur-based oxygen AOs contribute to the wave functions of HOMO−1 an HOMO−2 through σ-type antibonding interactions to the Ru($4d_{xz}$)-AO in the HOMO−2 and π-type antibonding interactions to the Ru($4d_{xy}$)-AO in HOMO−1. Upon formation of $RuSO_2$/SO, the degree of S character to the HOMO through HOMO−2 decreases significantly; the sulfinate and sulfenate are essentially nonbonding from a covalent perspective. Thus, the compound is becoming more ionic (i.e., the Ru center is becoming a harder Lewis acid).

Nitrogen contribution to the LUMO also increases upon thiolate oxygenation. The nitrogen that is strongly associated with this orbital is the axial nitrogen, which is consistent with the $4d_{z^2}$ identity of the metal-based orbital that is the primary contributor to the MO. There are also minor contributions from the equatorial nitrogen. The calculations show that the nitrogen contribution to the LUMO increases from 6.6% for RuS to 8.0% for $RuSO_2$ to 9.0% for $RuSO_2$/SO. The experimental N−K-edge data show an increase in the N character of the first excited state from 4.4 to 5.2 to 6.1% upon successive oxygenation. Owing to the paucity of available reference compounds to obtain estimates of I_N, the experimentally derived values for %N(2p) may be underestimated. Also, it is possible that the calculations have slightly overestimated the covalency of the Ru−N bonds. However, the trends and magnitudes of the experimental vs calculated nitrogen populations are nonetheless consistent with one another.

The calculated phosphorus K-edge data suggest a decrease in P character to both the LUMO (the P(3p) is antibonding to the $4d_{z^2}$; the a_1-type orbital) and the LUMO+4/6 (the P(3p) is antibonding to the $4d_{x^2-y^2}$; the b_1-type orbital). Upon oxygenation, the degree of P character to the LUMO drops dramatically; there is essentially no covalent bonding between the $4d_{z^2}$ and the P−σ based orbitals in $RuSO_2$/SO. This is consistent with the increase in P−Ru bond length upon sequential oxygenation, which in and of itself suggested that the phosphine ligand is more weakly bonding to the Ru center upon oxygenation of the thiolate sulfurs. Unlike the Ru−S bonds, where the loss of the covalent interaction between the Ru and the S is offset by a favorable reduction in π/π filled/filled electrostatic repulsion in the antibonding orbital, there is no such relief in unfavorable repulsive forces for the axial phosphine ligand in either $RuSO_2$ or $RuSO_2$/SO. Thus, the Ru−P bond elongates.

These observations are supported by a natural bonding orbital (NBO) analysis.[99−101] The natural bond occupancy of the Ru−S bond reduces from 1.75 for the Ru−thiolate *trans* to the amine nitrogen in RuS to 0.00 upon its conversion to a sulfinate in both $RuSO_2$ and $RuSO_2$/SO (i.e., those electrons are now bonding to the O atoms). For the Ru−S bond *trans* to the thioether, there is only a minor reduction in natural bond occupancy upon its conversion into a sulfenate; upon successive oxygenation of the complex, the Ru−S occupancy changes from 1.82 in RuS to 1.86 in $RuSO_2$ to 1.61 in $RuSO_2$/SO. The Ru−thioether natural bond occupancy remains virtually unchanged at 1.65 over the series. As the thiolate natural bond occupancy decreases, so does that of the Ru−P changing from 1.82 in RuS to 1.68 in $RuSO_2$ to 1.55 in $RuSO_2$/SO. The two donor electrons from the nitrogen atoms remain a virtual lone pair throughout the series. Thus, the complexes are becoming more ionic upon oxygenation.

Summary and Relevance to Nitrile Hydratase. NHases require oxygenated cysteinate residues to be catalytically active.[22] The functional reasons for these post-translational modifications are in debate. Herein, we have investigated the influence of sequential cysteinate oxygenation on a series of Ru(II) complexes (RuS, $RuSO_2$, and $RuSO_2$/SO). It had previously been observed crystallographically that upon sequential oxygenation of the thiolate sulfurs in these complexes the Ru−P bond length systematically increased.[39] The reason for this increasing length was not entirely clear.

In this study, we have demonstrated that the covalency of these complexes is largely dominated by Ru−S interactions, with the Ru−P and Ru−N interactions contributing to a lesser degree. Upon oxygenation, the covalent-bonding interactions between the oxygenated thiolates and the Ru center decreases. As this occurs, the overall covalency of the complexes decreases, and the charge on the Ru center increases as a result. The Löwdin atomic charge[97] on Ru increases from −0.073 in RuS to +0.0831 in $RuSO_2$ to +0.263 in $RuSO_2$/SO. In terms of hard/soft acid/base chemistry, the Ru center is becoming a harder Lewis acid. Thus, bonding between the progressively harder Ru center and the soft PPh_3 ligand would be expected to become weaker, which is what is observed. A recent series of crystal structures of Co-containing SCNase where the cysteinates have been sequentially oxygenated revealed a similar structural trend; as the cysteinates in SCNase become oxygenated from a thiolate to a monosulfinate and then to the sulfinate/sulfenate species, the bond length between the axial cysteinate sulfur and the Co(III) center increases.[9]

If a similar phenomenon is occurring in NHase (e.g., creation of a harder Lewis acid), then it should aid in nitrile hydrolysis. Currently, two mechanisms for nitrile hydrolysis are considered most likely. One mechanism involves the hydrolysis of a metal-

dx.doi.org/10.1021/ic202453c | Inorg. Chem. 2012, 51, 6032−6045

bound nitrile, which is currently the mechanism that has the most experimental/theoretical support, while the other involves attack from a metal-bound hydroxide to a free nitrile (Scheme 1). Our results seem to favor the second mechanism. In the case of the mechanism involving nitrile attack by the metal-bound hydroxide, the increased hardness would favor water coordination over coordination of a softer nitrile ligand. Furthermore, the increased charge on the metal center as a result of S-oxygenation would lower the pK_a of the coordinated water, generating the hydroxide for nitrile attack. The resulting amido product could then be displaced by a harder water ligand. We note, however, that a more acidic metal center would also aid in the mechanism involving a metal-bound nitrile by a free hydroxide. In this mechanism, the increased hardness of the metal would better polarize the nitrile CN bond aiding in attack by a free nitrile. Thus, an increase in the hard Lewis acidic nature of the metal ion would aid in catalysis regardless of the two mechanisms.

Scheme 1

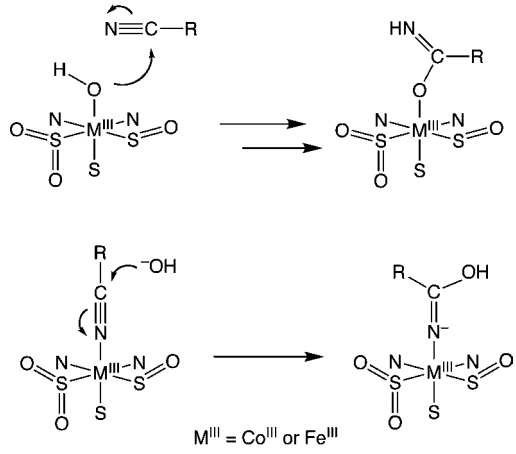

■ ASSOCIATED CONTENT

Supporting Information

Contains xyz coordinates for the three ruthenium complexes at B(38HF)P86 and BP86 levels of theory; N K-edge data for (bmmp-dmed)Ni; best fits to the sulfur K-edge data; ligand-field splitting diagram for RuS, $RuSO_2$, and $RuSO_2$/SO; plot of $\langle 1s|x|np\rangle$ vs I_{ion} with computational method description; additional N K-edge spectra, the second derivative of the P K-edge spectra; and ball and stick representations of the geometry optimized structures of the three complexes at the B(38HF)P86/TZVPP level of theory. This material is available free of charge via the Internet at http://pubs.acs.org.

■ AUTHOR INFORMATION

Corresponding Author

*E-mail: shearer@unr.edu; grapperhaus@louisville.edu.

Notes

The authors declare no competing financial interest.

■ ACKNOWLEDGMENTS

The authors thank the NSF (J.S., CHE-0844234; C.A.G., CHE-0749965) for financial support of this work. We also thank Prof. Serena DeBeer (Max-Planck-Institut für Bioanorganische Chemie) for helpful discussions. Use of the National Synchrotron Light Source, Brookhaven National Laboratory, was supported by the U.S. Department of Energy, Office of Science, Office of Basic Energy Sciences, under Contract No. DE-AC02-98CH10886.

■ REFERENCES

(1) Kovacs, J. A. *Chem. Rev.* **2003**, *104*, 823−848.
(2) De Santis, G.; Di Cosimo, R. *Biocatal. Pharm. Ind.* **2009**, 153−181.
(3) Kobayashi, M.; Shimizu, S. *Eur. J. Biochem.* **1999**, *261*, 1−9.
(4) Wieser, M.; Nagasawa, T. *Stereosel. Biocatal.* **2000**, 461−486.
(5) Harrop, T. C.; Mascharak, P. K. *Acc. Chem. Res.* **2004**, *37*, 253−260.
(6) Katayama, Y.; Nyunoya, H. *Baiosaiensu to Indasutori* **1999**, *57*, 387−390.
(7) Arakawa, T.; Kawano, Y.; Kataoka, S.; Katayama, Y.; Kamiya, N.; Yohda, M.; Odaka, M. *J. Mol. Biol.* **2007**, *366*, 1497−1509.
(8) Katayama, Y.; Hashimoto, K.; Nakayama, H.; Mino, H.; Nojiri, M.; Ono, T.-A.; Nyunoya, H.; Yohda, M.; Takio, K.; Odaka, M. *J. Am. Chem. Soc.* **2006**, *128*, 728−729.
(9) Arakawa, T.; Kawano, Y.; Katayama, Y.; Nakayama, H.; Dohmae, N.; Yohda, M.; Odaka, M. *J. Am. Chem. Soc.* **2009**, *131*, 14838−14843.
(10) Huang, W.; Jia, J.; Cummings, J.; Nelson, M.; Schneider, G.; Lindqvist, Y. *Structure* **1997**, *5*, 691−699.
(11) Miyanaga, A.; Fushinobu, S.; Ito, K.; Wakagi, T. *Biochem. Biophys. Res. Commun.* **2001**, *288*, 1169−1174.
(12) Nagashima, S.; Nakasako, M.; Dohmae, N.; Tsujimura, M.; Takio, K.; Odaka, M.; Yohda, M.; Kamiya, N.; Endo, I. *Nat. Struct. Biol.* **1998**, *5*, 347−351.
(13) Nakasako, M.; Odaka, M.; Yohda, M.; Dohmae, N.; Takio, K.; Kamiya, N.; Endo, I. *Biochemistry* **1999**, *38*, 9887−9898.
(14) Song, L.; Wang, M.; Shi, J.; Xue, Z.; Wang, M.-X.; Qian, S. *Biochem. Biophys. Res. Commun.* **2007**, *362*, 319−324.
(15) Throughout this manuscript, we use the term oxygenation to signify sulfur-based oxidation followed by oxygen-atom insertion. In contrast, oxidation signifies one-electron sulfur-based oxidation without oxygen atom insertion.
(16) Dey, A.; Chow, M.; Taniguchi, K.; Lugo-Mas, P.; Davin, S.; Maeda, M.; Kovacs, J. A.; Odaka, M.; Hodgson, K. O.; Hedman, B.; Solomon, E. I. *J. Am. Chem. Soc.* **2006**, *128*, 533−541.
(17) Lugo-Mas, P.; Dey, A.; Xu, L.; Davin, S. D.; Benedict, J.; Kaminsky, W.; Hodgson, K. O.; Hedman, B.; Solomon, E. I.; Kovacs, J. A. *J. Am. Chem. Soc.* **2006**, *128*, 11211−11221.
(18) Noguchi, T.; Nojiri, M.; Takei, K.-i.; Odaka, M.; Kamiya, N. *Biochemistry* **2003**, *42*, 11642−11650.
(19) Murakami, T.; Nojiri, M.; Nakayama, H.; Odaka, M.; Yohda, M.; Dohmae, N.; Takio, K.; Nagamune, T.; Endo, I. *Protein Sci.* **2000**, *9*, 1024−1030.
(20) Claiborne, A.; Mallett, T. C.; Yeh, J. I.; Luba, J.; Parsonage, D. *Adv. Protein Chem.* **2001**, *58*, 215−276.
(21) Stevens, J. M.; Belghazi, M.; Jaouen, M.; Bonnet, D.; Schmitter, J.-M.; Mansuy, D.; Sari, M.-A.; Artaud, I. *J. Mass Spectrom.* **2003**, *38*, 955−961.
(22) Tsujimura, M.; Odaka, M.; Nakayama, H.; Dohmae, N.; Koshino, H.; Asami, T.; Hoshino, M.; Takio, K.; Yoshida, S.; Maeda, M.; Endo, I. *J. Am. Chem. Soc.* **2003**, *125*, 11532−11538.
(23) Nojiri, M.; Yohda, M.; Odaka, M.; Matsushita, Y.; Tsujimura, M.; Yoshida, T.; Dohmae, N.; Takio, K.; Endo, I. *J. Biochem.* **1999**, *125*, 696−704.
(24) Shearer, J.; Callan, P. E.; Amie, J. *Inorg. Chem.* **2010**, *49*, 9064−9077.
(25) Mascharak, P. K. *Coord. Chem. Rev.* **2002**, *225*, 201−214.
(26) O'Toole, M. G.; Grapperhaus, C. A. *ACS Symp. Ser.* **2009**, *1012*, 99−113.
(27) Artaud, I.; Chatel, S.; Chauvin, A. S.; Bonnet, D.; Kopf, M. A.; Leduc, P. *Coord. Chem. Rev.* **1999**, *190−192*, 557−586.
(28) Bourles, E.; Alves de Sousa, R.; Galardon, E.; Giorgi, M.; Artaud, I. *Angew. Chem., Int. Ed.* **2005**, *44*, 6162−6165.

(29) Galardon, E.; Giorgi, M.; Artaud, I. *Chem. Commun.* **2004**, 286−287.
(30) Rat, M.; Alves de Sousa, R.; Vaissermann, J.; Leduc, P.; Mansuy, D.; Artaud, I. *J. Inorg. Biochem.* **2001**, *84*, 207−213.
(31) Kung, I.; Schweitzer, D.; Shearer, J.; Taylor, W. D.; Jackson, H. L.; Lovell, S.; Kovacs, J. A. *J. Am. Chem. Soc.* **2000**, *122*, 8299−8300.
(32) Lugo-Mas, P.; Taylor, W.; Schweitzer, D.; Theisen, R. M.; Xu, L.; Shearer, J.; Swartz, R. D.; Gleaves, M. C.; DiPasquale, A.; Kaminsky, W.; Kovacs, J. A. *Inorg. Chem.* **2008**, *47*, 11228−11236.
(33) Rose, M. J.; Betterley, N. M.; Mascharak, P. K. *J. Am. Chem. Soc.* **2009**, *131*, 8340−8341.
(34) Rose, M. J.; Betterley, N. M.; Oliver, A. G.; Mascharak, P. K. *Inorg. Chem.* **2010**, *49*, 1854−1864.
(35) Tyler, L. A.; Noveron, J. C.; Olmstead, M. M.; Mascharak, P. K. *Inorg. Chem.* **2003**, *42*, 5751−5761.
(36) O'Toole, M. G.; Kreso, M.; Kozlowski, P. M.; Mashuta, M. S.; Grapperhaus, C. A. *J. Biol. Inorg. Chem.* **2008**, *13*, 1219−1230.
(37) Grapperhaus, C. A.; Patra, A. K.; Mashuta, M. S. *Inorg. Chem.* **2002**, *41*, 1039−1041.
(38) Masitas, C. A.; Mashuta, M. S.; Grapperhaus, C. A. *Inorg. Chem.* **2010**, *49*, 5344−5346.
(39) Masitas, C. A.; Kumar, M.; Mashuta, M. S.; Kozlowski, P. M.; Grapperhaus, C. A. *Inorg. Chem.* **2010**, *49*, 10875−10881.
(40) Shearer, J.; Dehestani, A.; Abanda, F. *Inorg. Chem.* **2007**, *47*, 2649−2660.
(41) Hedman, B.; Frank, P.; Gheller, S. F.; Roe, A. L.; Newton, W. E.; Hodgson, K. O. *J. Am. Chem. Soc.* **1988**, *110*, 3798−3805.
(42) Engemann, C.; Franke, R.; Hormes, J.; Lauterbach, C.; Hartmann, E.; Clade, J.; Jansen, M. *Chem. Phys.* **1999**, *243*, 61−75.
(43) Gawelda, W.; Johnson, M.; de Groot, F. M. F.; Abela, R.; Bressler, C.; Chergui, M. *J. Am. Chem. Soc.* **2006**, *128*, 5001−5009.
(44) Vairavamurthy, A.; Wang, S. *Environ. Sci. Technol.* **2002**, *36*, 3050−3056.
(45) Chen, C. T.; Sette, F. *Rev. Sci. Instrum.* **1989**, *60*, 1616−162.
(46) Delgado-Jaime, M. U.; Mewis, C. P.; Kennepohl, P *J. Synchrotron Radiat.* **2010**, *17*, 132−137.
(47) Delgado-Jaime, M. U.; Kennepohl, P *J. Synchrotron Radiat.* **2010**, *17*, 119−128.
(48) Dey, A.; Jeffrey, S. P; Darensbourg, M.; Hodgson, K. O.; Hedman, B.; Solomon, E. I. *Inorg. Chem.* **2007**, *46*, 4989−4996.
(49) Stavitski, E.; de Groot, F. M. F. *Micron* **2010**, *41*, 687−694.
(50) Neese, F. N. *ORCA*; Universitat Bonn: Bonn, Germany, 2010.
(51) Schaefer, A.; Horn, H.; Ahlrichs, R. *J. Chem. Phys.* **1992**, *97*, 2571.
(52) The Ahlrichs (2df,2pd) polarization functions were obtained from the TurboMole basis set library under ftp.chemie.unikarlsruhe.de/pub/basen (accessed May 2012).
(53) Weigend, F.; Ahlrichs, R. *Phys. Chem. Chem. Phys.* **2005**, *7*, 3297−3305.
(54) Andrea, D.; Haeussermann, U.; Dolg, M.; Stoll, H.; Preuss, H. *Theor. Chim. Acta.* **1990**, *77*, 123−141.
(55) Perdew, J. P.; Chevary, J. A.; Vosko, S. H.; Jackson, K. A.; Pederson, M. R.; Singh, D. J.; Fiolhais, C. *Phys. Rev. A: Gen. Phys.* **1992**, *46*, 6671.
(56) Adamo, C.; Barone, V. *J. Chem. Phys.* **1998**, *108*, 664−675.
(57) Szilagyi, R. K.; Metz, M.; Solomon, E. I. *J. Phys. Chem. A* **2002**, *106*, 2994−3007 and references cited therein.
(58) Varetto, U. *Molekel*, v. 5.4.0.8; Swiss National Supercomputing Centre: Manno, Switzerland, 2009.
(59) Glendening, E. D.; Badenhoop, J. K; Reed, A. E.; Carpenter, J. E.; Bohmann, J. A.; Morales, C. M.; Weinhold, F. *NBO*, v. 5.0; Theoretical Chemistry Institute, University of Wisconsin: Madison, WI, 2001.
(60) DeBeer George, S.; Neese, F. *Inorg. Chem.* **2010**, *49*, 1840−1853.
(61) Pantazis, D. A.; Chen, X. Y.; Landis, C. R.; Neese, F. *J. Chem. Theory Comput.* **2008**, *4*, 908.
(62) Becke, A. D. *J. Chem. Phys.* **1993**, *98*, 5648−5652.
(63) Lee, C.; Yang, W.; Parr, A. D. *Phys. Rev. B* **1988**, *37*, 785−789.
(64) Vosko, S. H.; Wilk, L.; Nusair, M. *Can. J. Phys.* **1980**, *58*, 1200−1211.
(65) Stephens, P. J.; Devlin, F. J.; Chabalowski, C. F.; Frisch, M. J. *J. Phys. Chem.* **1994**, *98*, 11623−11627.
(66) Neese, F.; Wennmohs, F.; Hansen, A.; Becker, U. *Chem. Phys.* **2009**, *356*, 98−109.
(67) Kossmann, S.; Neese, F. *Chem. Phys. Lett.* **2009**, *481*, 240−243.
(68) Neese, F. J. *Comput. Chem.* **2003**, *24*, 1740−1747.
(69) van Lenthe, E.; Baerends, E. J.; Snijders, J. G. J. *Chem. Phys.* **1993**, *99*, 4597.
(70) Van Wüllen, C. *J. Chem. Phys.* **1998**, *109*, 382.
(71) Alperovich, I.; Smolentsev, G.; Moonshiram, D.; Jurss, J. W.; Concepcion, J. J.; Meyer, T. J.; Soldatov, A.; Pushkar, Y. *J. Am. Chem. Soc.* **2011**, *133*, 15786−15794.
(72) deGroot, F.; Kotani, A. *Core Level Spectroscopy of Solids*; Sarma, D. D., Kotliar, G., Tokura, Y., Eds.; CRC Press Taylor & Francis Group: Boca Raton, FL, 2008; Advances in Condensed Matter Science Vol. *6*.
(73) de Groot, F. *Chem. Rev.* **2001**, *101*, 1779−1808.
(74) de Groot, F. M. F. *Coor. Chem. Rev.* **2005**, *249*, 31.
(75) Hu, Z.; Kaindl, G.; Warda, S. A.; Reinen, D.; Degroot, F. M. F.; Muller, B. G. *Chem. Phys.* **1998**, *232*, 63.
(76) Hu, Z.; Mazumdar, C.; Kaindl, G.; Degroot, F. M. F.; Warda, S. A.; Reinen, D. *Chem. Phys. Lett.* **1998**, *297*, 321.
(77) Van der Laan, G.; Zaanen, J.; Sawatzky, G. A.; Karnatak, R.; Esteva, J. M. *Phys. Rev. B* **1986**, *33*, 4253−4263.
(78) Eskes, H.; Sawatzky, G. A. *Phys. Rev. B* **1991**, *43*, 119−129.
(79) deGroot, F. M. F. *J. Electron Spectrosc. Relat. Phenom.* **1994**, *67*, 529−622.
(80) Thole, B. T.; van der Laan, G. *Phys. Rev. B* **1988**, *38*, 3158−3171.
(81) Ralston, C. Y.; Wang, H.; Ragsdale, S. W.; Kumar, M.; Spangler, N. J.; Ludden, P. W.; Gu, W.l; Jones, R. M.; Patil, D. S.; Cramer, S. P. *J. Am. Chem. Soc.* **2000**, *122*, 10553−10560.
(82) Glaser, T.; Hedman, B.; Hodgson, K. O.; Solomon, E. I. *Acc. Chem. Res.* **2000**, *33*, 859−868.
(83) Shadle, S. E.; Hedman, B.; Hodgson, K. O.; Solomon, E. I. *J. Am. Chem. Soc.* **1995**, *117*, 2259.
(84) Solomon, E. I.; Hedman, B.; Hodgson, K. O.; Dey, A.; Szilagyi, R. K. *Coord. Chem. Rev.* **2005**, *249*, 97.
(85) Shadle, S. E.; Penner-Hahn, J. E.; Schugar, H. J.; Hedman, B.; Hodgson, K. O.; Solomon, E. I. *J. Am. Chem. Soc.* **1993**, *115*, 767.
(86) Because additional parameters were not added to the fits, we only considered a simple χ^2 analysis for evaluating the simulated data. Therefore, more sophisticated error analysis schemes that penalize the model for the inclusion of extra fitting parameters were deemed unnecessary.
(87) Neese, F.; Hedman, B.; Hodgson, K. O.; Solomon, E. I. *Inorg. Chem.* **1999**, *38*, 4854−4860.
(88) Shadle, S. E.; Hedman, B.; Hodgson, K. O.; Solomon, E. I. *Inorg. Chem.* **1994**, *33*, 4235−4244.
(89) Sarangi, R.; DeBeer George, S.; Rudd, D. J.; Szilagyi, R. K.; Ribas, X.; Rovira, C.; Almeida, M.; Hodgson, K. O.; Hedman, B.; Solomon, E. I. *J. Am. Chem. Soc.* **2007**, *129*, 2316−2326.
(90) Szilagyi, R. K.; Lim, B. S.; Glaser, T.; Holm, R. H.; Hedman, B.; Hodgson, K. O.; Solomon, E. I. *J. Am. Chem. Soc.* **2003**, *125*, 9158−9169.
(91) Sriskandakumar, T.; Petzold, H.; Bruijnincx, P. C. A.; Habtemariam, A.; Sadler, P. J.; Kenneepohl, P. *J. Am. Chem. Soc.* **2009**, *131*, 13355−13361.
(92) The reported errors are from a statistical analysis of the refined peak areas and do not necessarily reflect the errors in the actual covalencies.
(93) Bradley, J. A.; Yang, P.; Batista, E. R.; Boland, K. S.; Burns, C. J.; Clark, D. L.; Conradson, S. D.; Kozimor, S. A.; Martin, R. L.; Seidler, G. T.; Scott, B. L.; Shuh, S. K.; Tyliszczak, T.; Wilkerson, M. P.; Wolfsberg, L. E. *J. Am. Chem. Soc.* **2010**, *132*, 13914−13921.
(94) George, S. J.; Fu, J.; Guo, Y.; Drury, O. B.; Friedrich, S.; Rauchfuss, T.; Volkers, P. I.; Peters, J. C.; Scott, V.; Brown, S. B.;

Thomas, C. M.; Cramer, S. P. *Inorg. Chim. Acta* **2008**, *361*, 1157–1165.
(95) We note that the B3LYP hybrid-functional was used because low energy ghost states would creep into the calculations when the more cost-effective BP86 functional was used for the TD-DFT calculations.
(96) It has been demonstrated in reference 86 that the transition dipole integral for the "quasi-atomic" 1s → *n*p transition depends on the radial 1s and np functions. We find an excellent relationship between the calculated values obtained for $\langle 1s|x|np_x\rangle$ for Cl^-, S^-, S^{2-},and N and the experimentally derived values of I_{ion} (Supporting Information).
(97) Löwdin, P. O. *Adv. Quantum Chem.* **1970**, *5*, 185.
(98) Grapperhaus, C. A.; Darensbourg, M. Y. *Acc. Chem. Res.* **1998**, *31*, 451–459.
(99) Reed, A. E.; Weinstock, R. B.; Weinhold, F. *J. Chem. Phys.* **1985**, *83*, 735.
(100) Foster, J. P.; Weinhold, F. *J. Am. Chem. Soc.* **1980**, *102*, 7211.
(101) Reed, A. E.; Curtiss, L. A.; Weinhold, F. *Chem. Rev.* **1988**, *88*, 899.